MESO-SCALE MIXED-MODE FRACTURE MODELLING OF REINFORCED CONCRETE STRUCTURES SUBJECTED TO NON-UNIFORM CORROSION

Xun Xi[1, 2], Shangtong Yang[1*], Chun-Qing Li[3], Meifeng Cai[2], Xiaofei Hu[4], Zoe K. Shipton[1]

[1] *Department of Civil and Environmental Engineering, University of Strathclyde, Glasgow, G1 1XJ, United Kingdom.*

[2] *School of Civil and Resource Engineering, University of Science and Technology Beijing, Beijing, 100083, China.*

[3] *School of Engineering, RMIT University, Melbourne, Vic 3001, Australia.*

[4] *State Key Laboratory of Structural Analysis for Industrial Equipment, Dalian University of Technology, Dalian 116024, China.*

ABSTRACT

Corrosion-induced concrete cracking is a significant problem affecting the durability of reinforced concrete structures. Considerable research has been carried out in addressing this problem but few have considered the cracking process of concrete as a mixed-mode fracture and the concrete as a multi-phase material. This paper develops a meso-scale mixed-mode fracture model for the cracking of concrete structures under non-uniform corrosion of reinforcement. Concrete is treated as a three-phase heterogeneous material, consisting of aggregates, mortar and interfaces. An example is worked out to demonstrate the application of the derived model and is then partially verified against previously published experimental results. In agreement with experimental results, the new model reproduces the observation that microcracks tend to form first at the interfaces before they connect to generate a discrete crack. Toughening mechanisms, e.g., microcrack shielding, crack deflection, aggregate bridging and crack overlap, have been captured in the model. Further, effects of aggregate randomness on the crack width development of concrete structures, differences between uniform and non-uniform corrosion and a comprehensive parametric study have been investigated and presented.

Keywords: non-uniform corrosion, cohesive crack model, meso-scale, reinforced concrete structures, finite element method.

* Corresponding author. Tel: +44 141 548 3273. Email: shangtong.yang@strath.ac.uk.

1 INTRODUCTION

Reinforced concrete (RC) structures are widely used in civil engineering buildings, bridges, retaining walls, tunnels, piers, etc. However, in environments rich in chloride (Cl^-) and carbon dioxide (CO_2), the reinforcement in concrete is prone to corrosion. Deterioration induced by corrosion of reinforcement is the greatest threat to the durability and service life of civil engineering structures. Worldwide, the maintenance and repair costs for corrosion-affected concrete infrastructure are estimated around \$100 billion per annum [1]. In the context of climate change, the corrosion problem for RC structures and infrastructures is likely to be exacerbated. Therefore, there is a well justified need for a thorough investigation of the corrosion-induced cracking process, not least bearing in mind that the determination of crack width is essential to the prediction of the serviceability of corrosion-affected RC structures and to decision making regarding the repairs for the structures [2].

To model the corrosion-induced cracking of concrete, analytical methods have been often employed to predict the time to surface cracking [3-6], crack patterns [7, 8] and crack width development [2, 9]. Analytical models are rigorous in terms of mathematical formulation and can be easily applied in engineering applications. However, the boundary conditions that can be applied are limited and it is nearly impossible to predict the development of fractures through multi-phase materials, which retards the widespread application of the analytical method. Instead, researchers have resorted to numerical method for the problem of concrete cracking induced by reinforcement corrosion [10-18]. For example, Chen and Leung simulated concrete cover cracking by non-uniform corrosion of rebars of different locations within a concrete structure by inserting cohesive elements into predefined crack paths; different displacement boundary conditions were applied on two sides of geometries [19]. Xi and Yang modelled concrete cracking caused by non-uniform corrosion of multiple rebars and found that short spacing between rebars could cause delamination of the whole cover [20]. In most of these models, concrete is considered as a homogenous quasi-brittle material. The assumption of heterogeneity is flawed: concrete is a heterogeneous material at the meso-scale, consisting of aggregate particles, mortar and interfaces (usually known as ITZ). Šavija et al. [21] and Chen et al. [22] used a 2D heterogeneous lattice model to simulate the crack propagation and crack width development of concrete induced by linear decrease non-uniform corrosion model, and found when pitting corrosion occurs, significantly less total pressure is needed to crack the concrete cover compared to uniform corrosion. Du et al. [23] employed the damage plastic model to simulate failure of side-located and corner-located reinforcing bars under non-uniform corrosion by assuming the concrete as a three-phase material but only failure patterns and pressure are discussed.

Almost all numerical models have considered corrosion-induced cracking of concrete as a problem of tensile cracking [19, 21, 24] (i.e., Mode I) or combined tensile cracking and compression damage [12, 13, 23]. The shear fracture (Mode II) of concrete has seldom been considered. Acoustic emission experiments on corrosion-induced concrete cracking have revealed that both Mode I and Mode II fracture mechanisms existed during the crack propagation, and the contribution of individual modes into the global fracture behaviour varies [25]. This is because, for the heterogeneous concrete, mixed-mode fracture will occur when cracks roughly propagating. In particular, under non-uniform corrosion as illustrated in Figure 1, both normal and shear stresses develop in around the corroded part of the reinforcement. It therefore becomes necessary to consider the corrosion-induced concrete cracking as a mixed-mode fracture process, rather than Mode I fracture only. Given very limited literature on mixed-mode fracture simulation of concrete caused by corrosion of reinforcement, we conducted a review on mixed-mode fracture simulation for other concrete structures. Gálvez et al. [26] investigated the influence of shear properties on mixed-mode fracture of concrete based on experimental results and macro-scale numerical analysis. They have found that cracking of concrete beams under bending tests is initiated under mixed-mode but propagates under Mode I. Luciani et al. [27] discussed the constitutive model of cohesive element for mixed-mode fracture [28] and investigated the effects of Mode II fracture parameters on mixed-mode fracture of concrete at macro-scale; it has been found that Mode II parameters can change in a large range without noticeable change in results. Yang and Xu [29] built a heterogeneous cohesive model for four-point single-edge notched shear beam based on meso-scale random fields of fracture properties and found that simulations considering the shear fracture resistance showed a noticeable increase in the structural ductility or toughness over homogeneous models. The existing literature on mixed-mode fracture of concrete has not considered concrete as a multi-phase material in which case the toughening behaviour of aggregates and the weakening effect of interfaces cannot be simulated. Further, for corrosion-induced (non-uniform) cracking of concrete at meso-scale, the stress state is more complicated but so far there is no model which can fully address the mixed-mode fracture of heterogeneous concrete under (non-uniform) corrosion of reinforcement.

This paper attempts to develop a meso-scale mixed-mode fracture model for reinforced concrete structures subjected to non-uniform corrosion. Concrete is treated as a three-phase heterogeneous material, consisting of aggregates, mortar and interfaces. In order to model arbitrary discrete cracking of concrete, cohesive crack elements are inserted into the mesh for all the phases, through an in-house script written in Python. A constitutive model for mixed-mode fracture is introduced and discussed. An example is presented to demonstrate the application of the derived model and the model is partially verified through comparison with experimental results from the literature. We show that our model captures different toughening mechanisms in concrete at the meso-scale. Repeatability of results and effects of randomness are also discussed. Further, the contribution of shear in the fracture behaviour of concrete under non-uniform corrosion expansion is examined. Finally, a parametric study is presented, investigating the effects of some underlying parameters, e.g., shear fracture energy, interface strength, cover thickness and uniform corrosion, on the crack pattern and the development of crack width.

2 NON-UNIFORM CORROSION MODEL

When the reinforcement in concrete is corroded, the higher-volume corrosion products will accumulate and push the surrounding concrete outwards which can cause cracking and delamination of RC structures. As shown in Figure 1, ϕ is the diameter of the reinforcing bar and d_0 is the thickness of the annular layer of concrete pores at the interface between the bar and concrete, often referred to the “porous zone” [3] or “corrosion accommodation zone” [30]. Usually d_0 is constant once concrete has hardened. In this study, d_0 is assumed 12.5 μm [31]. Depending on the level of corrosion, the products of corrosion may occupy up to several times more volume than the original steel [21]. It is assumed that no stress is produced and exerted on the concrete until the “porous zone” around the reinforcement is fully filled by the corrosion products. As the corrosion products proceed further in concrete, a band of corrosion products forms, as shown in Figure 1. It has been found that the front of corrosion products for the half of the rebar facing concrete cover is in a semi-elliptical shape, while corrosion of the inward-facing half of rebar is negligibly small and can be neglected [32].

As illustrated in Figure 1, there may be three bands accommodating the corrosion products: the semi-elliptical band of corroded steel with maximum thickness d_{co-st}, the semi-elliptical rust band with maximum thickness d_m (also referred to as corrosion expansion displacement in this paper) and the circular band of porous concrete, d_0. The front of the corrosion is in a semi-elliptical shape with the semi-major axis equal to $\phi/2+d_0+d_m$ and the semi-minor axis equal to $\phi/2+d_0$.

By considering the original location of inner boundary of the concrete, i.e., $\phi/2+d_0$, the displacement boundary condition of the concrete structure $r(\theta)$ can be derived as follows,

$$r(\theta)=\frac{(\phi+2d_0+2d_m)(\phi+2d_0)}{\sqrt{(2\phi+4d_0)^2+16d_m(\phi+2d_0+d_m)\cos^2\theta}}-\frac{\phi}{2}-d_0 \tag{1}$$

where $0\le\theta\le\pi$.

Further, the relationship between maximum corrosion displacement d_m, as shown in Figure 1(b), and corrosion degree η can be derived as follows:

$$d_m=\frac{\eta\rho_{st}\phi}{\alpha_{rust}}\left(\frac{1}{\rho_{rust}}-\frac{\alpha_{rust}}{\rho_{st}}\right)-2d_0 \tag{2}$$

ρ_{rust} is the density of corrosion products, ρ_{st} is the density of steel bar and α_{rust} is the molecular weight of steel divided by the molecular weight of corrosion products. Details of the derived non-uniform corrosion model can be found in the authors' previous studies [8, 20] while it is not repeated herein. It should be mentioned that, the non-uniform corrosion model is derived from accelerated corrosion experiments exposed to chloride-rich environment [32].

3 CONCRETE CRACK MODEL

3.1 Meso-scale discrete crack model of concrete

In this paper, concrete is modelled as a three-phase material (i.e., consisting of aggregates, mortar and ITZ). In our model the shape of aggregate particles is simplified to a randomly sized and oriented polygon with 3 to 7 sides. The aggregate size distribution can be represented by a grading curve, which is usually expressed in terms of cumulative percentage passing through a series of sieves with different opening sizes. A typical gradation of aggregate size distribution is listed in Table 1 [33]. For simplicity, only coarse aggregates larger than 2.4 mm are modelled in this study, while fine aggregates and cement are treated as mortar phase. Coarse aggregates generally occupy 40% of the whole volume of concrete. The basic process of generating the multi-phase structure meso-scale is to produce and place different aggregate particles in a repeated and random manner in the target area until it reaches 40% of the area of the grid. First, an aggregate is generated with 3-7 sides and a random size in specified grading segments. Then the aggregate is placed in the target area with a random position. There is a minimum distance between aggregates and boundary. More aggregates are generated and placed one by one until the total fraction of aggregates in the grading segments reaches the specified value. There is no overlapping of aggregates in the generating process. The remaining area becomes the target area for next smaller grading segments and the procedures are repeated until the last aggregate of smallest size is generated and placed. The 3-phase structure is generated from a Python script that populates drawings in AutoCAD; the structure is then imported into ABAQUS FE software for analysis.

To model arbitrary cracking in concrete, cohesive elements are embedded at the interfaces throughout the mesh. A very fine mesh is produced to ensure random crack paths. The insertion process of cohesive elements is shown in Figure 2. First, all individual nodes are replaced by certain number of new nodes at the same location. The number of newly created nodes depends on the number of elements connecting to the original node. Second, the newly created nodes at the interface between two triangle elements are identified and linked to form a cohesive element. The cohesive elements are shown in red in Figure 2. The cohesive elements are generated by an in-house Python script. Figure 3 shows the inserted cohesive elements at the interfaces of aggregates and mortar, as well as the aggregates and the mortar themselves. The developed model is capable of simulating crack propagation and opening both at the interface and in the bulk mortar and aggregates, depending on their mechanical properties.

3.2 Mixed-mode fracture model

The cohesive crack model was first proposed by Hillerborg et al in 1976 [34] to model discrete cracks and energy dissipation in the fracture process zone (FPZ) of concrete. Normally, the cohesive element is of zero thickness to simulate the cracking of concrete; therefore, a traction-separation law is usually employed to constitutively control the cohesive elements. The traction of cohesive elements is a function of the corresponding relative displacements of the crack surface. In general, the traction-separation laws for mode I and mode II fracture can be expressed respectively as follows:

$$\begin{aligned} \sigma_n &= f_n(\delta_n) \\ \sigma_t &= f_s(\delta_s) \end{aligned} \tag{3}$$

where σ_n and σ_t are the normal traction and tangential traction, respectively; δ_n and δ_s are the crack opening displacement and crack sliding displacement; f_n and f_s are the non-linear functions defining the relationships between traction and separation for mode I and mode II fracture, respectively.

However, due to complex loading condition, material heterogeneity and aggregate interlocking etc., in most cases, cracks propagate in concrete under mixed-mode condition rather than in the single mode. Before the damage initiation, the normal stress σ_n and shear stress σ_t have a linear relationship with the crack opening displacement δ_n and crack sliding displacement δ_s, which can be expressed as follows:

$$\begin{aligned} \sigma_n &= K_p < \delta_n > \\ \sigma_s &= K_p \delta_s \end{aligned} \tag{4}$$

where < > is the Macaulay bracket and the normal stress equals to zero for compression condition. K_p is the penalty stiffness of the cohesive element. The concept of penalty stiffness evolves from the elastic stiffness which is obtained by dividing the elastic modulus of the concrete by its thickness. Since cohesive interface is normally very thin or of zero thickness, the elastic stiffness of the cohesive interface approaches infinitesimally large. This makes sense as the interface should be stiff enough prior to the initiation of crack to hold the two surfaces of the bulk concrete together, leading to the same performance as if of no interface existed. Therefore, the cohesive stiffness becomes a ‘‘penalty” parameter (K_p), which controls how easily the cohesive interface deforms elastically. As such this stiffness is large enough to provide the same or close response of intact concrete prior to cracking, but not so large as to cause numerical problems [24, 35, 36].

A quadratic stress damage criterion is employed to determine the beginning of damage. The damage initiation law is expressed as follows:

$$\left(\frac{< \sigma_n >}{\sigma_n^0} \right)^2 + \left(\frac{\sigma_s}{\sigma_s^0} \right)^2 = 1 \tag{5}$$

where σ_n^0 and σ_s^0 are the tensile and shear cohesive strength of concrete, respectively.

By using the same value of penalty stiffness K_p, the damage criterion can also be expressed as follows:

$$\left(\frac{<\delta_n>}{\delta_n^0}\right)^2 + \left(\frac{\delta_s}{\delta_s^0}\right)^2 = 1 \tag{6}$$

where δ_n^0 and δ_s^0 are the critical displacement for mode I and mode II fracture, respectively. δ_n^0 and δ_s^0 can be calculated by dividing the corresponding cohesive strength to the penalty stiffness K_p. If the tensile strength is the same as shear strength, the function becomes a circle with radius δ_n^0 or δ_s^0.

After the stress state meets the damage initiation criterion, the normal and shear stress decrease gradually while the responding displacement continues to increase. Such stiffness degradation behaviour is known as strain softening. For mixed-mode fracture, the damage is characterised by one scalar variable *D* representing the overall damage of the crack. For 2D plane problem, the total mixed-mode effective relative displacement δ_m is introduced as:

$$\delta_m = \sqrt{<\delta_n>^2 + \delta_s{}^2} \tag{7}$$

For linear softening, the expression for the damage model is given as follows:

$$D = \frac{\delta_{m,f}\left(\delta_{m,\max} - \delta_{m,0}\right)}{\delta_{m,\max}\left(\delta_{m,f} - \delta_{m,0}\right)} \tag{8}$$

where $\delta_{m,\max}$ is the maximum effective relative displacement during the loading history. $\delta_{m,0}$ is the critical effective relative displacement when the damage starts (i.e., *D*=0). $\delta_{m,f}$ is the effective relative displacement when complete failure occurs (i.e., *D*=1). The B-K failure criterion proposed by Benzeggagh and Kenane [37] is used to capture the mixed-mode facture for different composite and quasi-brittle materials [28]. According to the B-K failure criterion, $\delta_{m,f}$ can be expressed as follows:

$$\delta_{m,f} = \frac{2}{K_p \delta_{m,0}} \left[G_I + \left(G_{II} - G_I \right) \left(\frac{G_s}{G_n + G_s} \right)^{\eta} \right] \tag{9}$$

where G_I and G_{II} are the fracture energy of mode I and mode II, respectively. G_n and G_s are the work done by the tractions and their conjugate relative displacements in the normal, shear directions, respectively. η is a characteristic parameter of materials, which can be set as 2 for composite quasi-brittle materials [28].

The mixed-mode fracture energy G_C can be expressed as follows:

$$G_C = \left[G_I + \left(G_{II} - G_I \right) \left(\frac{G_s}{G_n + G_s} \right)^{\eta} \right] \tag{10}$$

Clearly, for mode I fracture, $G_s = 0$ and the contribution of shear on fracture (i.e., $G_s/(G_n + G_s)$) is zero. For mode II fracture, $G_n = 0$ and the contribution of shear on fracture (i.e., $G_s/(G_n + G_s)$) is 1.

Once the damage variable D is determined, the residual normal and shear stresses can be obtained by:

$$\begin{aligned} \sigma_n &= (1-D) K_p \delta_n \\ \sigma_s &= (1-D) K_p \delta_s \end{aligned} \tag{11}$$

If the overall damage variable D reaches 1, the normal and shear stresses are zero and the cohesive element completely fails.

Figure 4(a) illustrates the response model for mixed-mode fracture. It can be seen that, before damage initiation, the normal, shear and effective stresses increase linearly by a slope equivalent to the penalty stiffness. When the effective displacement (i.e., Equation 7) reaches the inner ellipse shown in the $\delta_s - \delta_n$ plane in Figure 4(a) with semi-major axis δ_s^0 and semi-minor axis δ_n^0, the damage is initiated and the stresses begin to decrease. For mixed-mode fractures the fracture energy varies depending on the relative contributions of Mode I and Mode II. Figure 4(b) shows a special case for mixed-mode fracture when the shear and tensile strengths are same and fracture energies for mode I and mode II are the same. In this case, the damage initiation ellipse becomes a circle with the radius equal to the strength. Moreover, the mixed-mode fracture energy is equal to that of single mode fracture and the effective relative displacement to complete failure will not change with the mixed-mode ratio.

4 WORKED EXAMPLE

We demonstrate the application of the developed numerical method and techniques in solving non-uniform corrosion induced concrete cracking through a worked example. The values for all parameters are shown in Table 2, together with their sources. As in previous studies [26, 38, 39], the shear fracture properties are hard to identify due to the lack of experimental data. Some researchers assume the shear properties are the same as the normal ones (i.e., $\sigma_n^0 = \sigma_s^0$ and $G_I = G_{II}$) [38, 40, 41]. Some researchers postulated that shear properties have little effect on corrosion induced concrete cracking and only mode I fracture is considered in their model [12, 19, 42]. However, for a heterogeneous model with rough fracture surfaces, it is necessary to consider the effect of shear properties on concrete cracking. Experimental results on concrete samples indicated that the shear strength is greater than or equal to the tensile strength and the fracture energy for mode II is greater than that of mode I [26, 27]. Thus, in our model the shear strength is assumed the same as the tensile strength and the fracture energy for model II is twice that for mode I. Another important aspect for meso-scale fracture modelling of concrete is the fracture properties of ITZ. Experimental results indicated that the tensile strength of ITZ is about 1/16th to 3/4 of the strength of the mortar matrix [42-46]. Accordingly the tensile strength of ITZ is set to half the tensile strength of the mortar matrix in this example. The average ratio of fracture energy G_I to tensile strength (i.e., average failure displacement) is about 0.013 mm in the experimental results from Rao and Prasad [44]. We therefore assume in our case study that the value of facture energy G_I for ITZ is 0.013 times the tensile strength value of ITZ. The shear strength of ITZ is assumed the same as tensile strength of ITZ and the fracture energy for mode II is twice that of mode II. The mechanical properties of aggregates are normally considerably stronger than mortar and the ITZ; thus it is very rare to have a crack breaking through an aggregate. In this paper, fracture properties are only assigned in the ITZ and mortar, to reduce computational cost.

Figure 5 shows the typical mesh of the meso-scale RC cover structure with a middle rebar. The size of the RC structure is set 150×150 mm and the thickness of concrete cover is 40 mm. The average size of elements in the mesh is about 1.6 mm, which is fine enough to simulate arbitrary cracks while keeping computational time reasonable. The non-uniform corrosion model developed in Section 2 is used to define the displacement boundary condition at the interface between the corroded rebar and the concrete.

Figure 6 shows the crack propagation process induced by non-uniform corrosion of reinforcement. Cohesive elements with damage variable D equal to 1 (i.e. complete failure) are plotted in red. In order to more clearly illustrate the crack geometries and opening, the size of elements deformation is exaggerated by 10. It can be found that a few micro cracks are first initiated at the aggregate-mortar interfaces near the upper surface of the concrete cover. As corrosion continues, the micro cracks are then connected to form a dominant crack propagating from the concrete surface to the rebar. The phenomenon of the crack propagating from concrete surface towards the reinforcement is in good agreement with experiments [47]. As corrosion continues, two further cracks appear on the lateral margins of the corroded rebar, as shown in Figure 6. Unlike macro-scale fracture modelling which normally considers concrete as a homogeneous material, the meso-scale model can simulate the micro cracks which always form first at the ITZ before they are connected to become a macro-scale discrete crack. This is because the strength and fracture energy of ITZ cohesive elements are significantly lower than those of mortar. Figure 7 illustrates the microcrack shielding, crack deflection and aggregate bridging phenomena that have previously been very challenging to simulate [20]. There are many microcracks appearing near the area of stress concentration where the corrosion has developed furthest. Some of the microcracks will propagate, connect and form a through-going crack. Crack deflection occurs when the potential crack path of least resistance is around an aggregate or a weak interface. Aggregate bridging occurs when the crack propagates along two sides of an aggregate and advances beyond the aggregate. As such, the developed meso-scale fracture model is advantageous compared with most existing concrete fracture models [19, 29] in terms of capturing toughening mechanisms and crack propagation.

As introduced in the constitutive model for mixed-mode fracture and mechanical parameters in this example, the shear strength is the same as tensile strength, and fracture energy for mode II is greater than that for mode I. Thus, the effective displacement to damage initiation for mixed-mode fracture is equal to that for the single mode I and mode II fracture. The higher the component of shear in a mixed-mode fracture, the larger the fracture energy is. Figure 8 illustrates the relative contribution of shear fracture energy for the different cracked elements which form the discrete cracks. In these models, the contribution of shear on the fractures varies from about 0 to 0.9 during crack propagation (0 means Mode I fracture while 1.0 means Mode II fracture). Most values for the contributions of shear are less than 0.5, which indicates that the crack propagation is mixed-mode but mode I is dominant. It is interesting to note that the higher contributions of shear occur where cracks have deflected round aggregates, which indicated that more energy is required for the cracks bypassing the aggregates.

For the heterogeneous concrete model, the aggregates are randomly generated but following the same volume fraction, grading, size, etc. The effect of meso-scale randomness on crack pattern and crack width should be investigated. Figure 9 shows the corrosion induced crack patterns induced under four typical random meso-scale models. It can be seen that, three discrete cracks, i.e., one top crack and two side cracks, always form around the reinforcing bar. The crack patterns are quite similar in the four models, however, different shapes, size and location of aggregates lead to cracks with different morphologies. For example, the cracked elements at the upper discrete crack in model 2 are deformed with more tangential displacement because of the presence of the large aggregate particle. It is interesting to find that crack overlap occurs when two approximately parallel cracks propagate from weak interfaces and interact with a variable overlap distance.

By measuring the distance between the two nodes of the surface cohesive element, the crack width development on the concrete surface under the maximum corrosion displacement d_m can be schematically illustrated. It should be noted that this distance obtained initially represents the displacement of the surface cohesive element (often referred to as cohesive/fictitious crack width); after the complete failure of this element, the distance measured represents the true surface crack width. Figure 10 illustrates the crack width development with maximum corrosion displacement d_m. It can be found that the crack width initiates when d_m increases to about 0.015 mm followed by a roughly linear increase of crack width. The surface crack initiation occurs in a similar location above the corroded rebar irrespective of meso-scale randomness, but the final crack width depends on the random arrangement of the aggregate particles. This is reasonable because the aggregate distribution will affect the mixed-mode fracture energy and the crack morphology has effect on crack width. For example model 2 has the smallest crack width in Figure 9 because the contribution of shear on the upper crack is greater. In general, the meso-scale fracture model in this study has a good repeatability.

5 VERIFICATION

To verify the proposed numerical method, the results are compared with experimental results from Andrade et al [48]. According to the literature, most experimental test data are based on uniform corrosion of reinforcement generated by electric current method for producing accelerated corrosion. It would be ideal to compare directly the results between the developed model and experiments under non-uniform corrosion; however, the data on non-uniform corrosion is rather scarce. Additionally, almost all the experiments use an electric current to generate corrosion which, while producing results quickly, only produces generally uniform corrosion. In this paper, a uniform corrosion case is conducted by the derived model and the results are compared with those in [48] for partial verification. The values for basic parameters are presented in Table 3. It should be noted that the thickness of the "porous zone" between concrete and rebar is considered as 12.5 μm in the numerical simulation. The experimental results of crack width were expressed as a function of the radius loss of rebar. For the sake of comparison with the numerical results, the uniform corrosion displacement is transformed to radius loss of rebar. The relationship between uniform corrosion expansion displacement $d_{m,u}$ and radius loss of rebar ΔR can be expressed as follows:

$$d_{m,u} = \left(\frac{\rho_{st}}{\rho_{rust} \times \alpha_{rust}} - 1 \right) \times \Delta R - d_0 \tag{12}$$

The comparisons of the crack width from the developed numerical model and the experimental data of Andrade et al [48] are illustrated in Figure 11. The progress of the simulated crack width is in reasonably good agreement with the experimental results. It should be mentioned that the crack width from the experiments was measured by strain gauges; how the measured strains were transformed by Andrade et al [48] to crack width was not quite clear. However, the crack width from the numerical model was obtained by calculating the displacement of the surface cohesive element. The different method used for attaining the crack width might cause some minor difference in the results between the experiment and the numerical model. Moreover, it has been found that the crack width from the numerical model is slightly larger than that from the experiment. It is perhaps caused by the 2D plain strain assumption in the model since constraint effect in the third dimension is ignored and more complicated toughening mechanism exists in the real case.

6 PARAMETRIC STUDY AND DISCUSSION

As demonstrated in Figure 8, the Mode II fracture energy has a varying contribution to the mixed-mode fracture. The effect of mode II fracture energy on concrete cracking induced by non-uniform corrosion is investigated. Figure 12 shows the crack patterns of concrete cover under different shear fracture energy scenarios. The same fracture energy for mode I fracture is used in the simulations. It can be seen that crack patterns are similar when the mode II fracture energy varies from 2 times mode I fracture energy to 20 times (Figure 12 b,c,d). However, the crack patterns have significant changes when the mode II fracture energy is the same or 100 times of the mode I fracture energy (Figure 12 a and e). For $G_{II} = G_I$, the cracked elements in the three main cracks have larger tangential (i.e., shear) displacement than in the other cases, and the discrete crack path tends to form along ITZs. In such a failure, mode II shear mechanism plays an important role. For a relatively large value, i.e., $G_{II} = 100G_I$, the failed elements (in red) in the discrete cracks are all in mode I fracture; some elements with larger tangential displacement (in yellow box) are damaged but not completely failed because of the large mode II fracture energy. The greater the contribution of shear on a mixed-mode fracture, the more energy is required to form a discrete crack and the shear displacement becomes ductile after damage initiation. Figure 13 illustrates the crack width development under different fracture energies for mode II fracture. It can be found that the smaller the mode II fracture energy, the faster the crack width increases. The drop lines show complete failure of the first cracked cohesive element at surface of concrete. For mixed-mode fracture, the surface cracking time and complete failure displacement of cohesive element vary with the fracture energy of Mode I and Mode II and their contributions on facture. It can be seen in Figure 13, the larger the G_{II} is, the later the complete failure occurs (i.e., surface cracking). However, the value of G_{II} in the range of 2-20 times of G_I has little effect on the crack width development. Therefore, for mixed-mode fracture of concrete, the mode II fracture energy has little influence on crack width development when it is a relatively reasonable larger value than mode I fracture energy; but the shear fracture parameters should not be ignored or regarded as the same as mode I fracture energy, especially for meso-scale fracture modelling of concrete.

The effects of strength of ITZ on concrete cover cracking are investigated using different ratios of tensile and shear strengths of ITZ to these of mortar. The ratios of mode I fracture energy to tensile strength and mode II fracture energy to shear strength are kept constant. Figure 14 shows the crack patterns affected by the strength of ITZ. It can be seen that, the lower the strength of ITZ, the more cracks form along the ITZs. When the strength of ITZ is 1/8th of the mortar, there are more intermittent discrete cracks appearing at the weak zones of ITZ than in the simulations where the ITZ are stronger. Figure 15 illustrates the crack width development under different values of ITZ strength. It can be found that, the lower the ITZ strength, the larger the crack width. For example, when d_m reaches 0.2 mm (corrosion degree of steel bar is 0.64%), the crack width for strength of ITZ 1/8th that of mortar is 0.3 mm which is 30% larger than the crack width for strength of ITZ 3/4 of that of mortar. Therefore, it is important to improve the strength of ITZ for durability of RC structures.

Figure 16 shows the crack patterns of concrete cover affected by cover thickness. It can be seen that, for thinner cover, the side cracks have a tendency to propagate towards the surface and thus the volume of cover that may spall from the concrete surface smaller. The concrete thickness has little effect on the position of the upper crack. Figure 17 illustrates the crack width development for different cover thicknesses. As expected, the thicker the cover is, the later the cohesive crack width increases. It is interesting to find that once the surface is cracked, the crack width becomes larger when the cover thickness is larger. It is probably because the corresponding strain at the surface for larger cover thickness induced by non-uniform corrosion products expansion is larger. However, it should be mentioned that, a thicker cover will delay the time to corrosion initiation which is not considered in the model.

Thus, a thicker cover should still delay the time to surface cracking; however, after the surface of concrete cover is cracked, the crack width will increase faster for thicker cover.

Most previous studies about corrosion-induced concrete cracking have been based on uniform corrosion. It is necessary to compare the difference of concrete cracking between uniform corrosion and non-uniform corrosion. Figure 18 shows the uniform corrosion induced crack patterns for cover thickness 20 mm and 40 mm. For uniform corrosion, two discrete cracks form vertically and the top crack has a larger crack width, which is consistent with experimental results from [48]. Figure 19 illustrates the crack width affected by corrosion model and cover thickness. It can be found that, the crack widths for non-uniform corrosion begin increasing earlier than those for uniform corrosion. This is mainly because for uniform corrosion, more corrosion products are required to fill in the "porous zone" between concrete and reinforcement. Moreover, the crack width induced by non-uniform corrosion is larger than that by uniform corrosion. The thicker the cover is, the larger the difference of crack width between non-uniform and uniform corrosion. Therefore, the models based on uniform corrosion of reinforcement overestimate the time to surface cracking and crack width, especially for thicker cover cases.

7 CONCLUSIONS

In this paper, a meso-scale mixed-mode model has been developed to simulate discrete crack propagation in concrete and to predict the crack width induced by corrosion of reinforcement. A non-uniform corrosion model was first described based on previous experimental results. A three phase (i.e., aggregates, mortar and interfaces) heterogeneous concrete model was considered and a mixed-mode fracture model was formulated. It has been found that microcracks tend to form first at the ITZ before they connect to generate a discrete crack.

Some toughening mechanisms were also captured, e.g., microcrack shielding, crack deflection, aggregate bridging and crack overlap. Further, the effect of aggregate randomness on crack width development of concrete was investigated. The developed model was partially verified by comparing the results with those from experiments. A parametric study was carried out to examine the effects of some underlying parameters, e.g., shear fracture energy, ITZ strength, cover thickness and uniform corrosion, on the crack pattern and the development of crack width. Moreover, the models based on uniform corrosion of reinforcement overestimated the time to surface cracking and underestimated the crack width, especially for thicker cover. It can be concluded that the numerical model presented in the paper can be used to simulate the meso-scale fracture of concrete structures which is subjected to non-uniform corrosion of reinforcement.

ACKNOWLEDGEMENTS

Financial support from European Commission via the Marie Sklodowska-Curie H2020 RISE scheme under 645696 and National Key R&D Plan of China (Grant No: 2016YFC0600803) are gratefully acknowledged. Part computational results were obtained by using ARCHIE-WeSt High Performance Computer. The first author would also like to thank China Scholarship Council for supporting his PhD research at the University of Strathclyde, UK.

REFERENCES

[1] Li CQ, Yang ST. Prediction of concrete crack width under combined reinforcement corrosion and applied load. J Eng Mech. 2011;137:722-31.
[2] Li CQ, Melchers RE, Zheng JJ. Analytical model for corrosion-induced crack width in reinforced concrete structures. ACI Structural Journal. 2006;103:479-87.
[3] Liu Y, Weyers RE. Modelling the time-to-corrosion cracking in chloride contaminated reinforced concrete structures. ACI Mater J. 1998;95:675-81.

[4] Bhargava K, Ghosh AK, Mori Y, Ramanujam S. Model for cover cracking due to rebar corrosion in RC structures. Eng Struct. 2006;28:1093-109.
[5] Lu C, Jin W, Liu R. Reinforcement corrosion-induced cover cracking and its time prediction for reinforced concrete structures. Corros Sci. 2011;53:1337-47.
[6] El Maaddawy T, Soudki K. A model for prediction of time from corrosion initiation to corrosion cracking. Cem Concr Compos. 2007;29:168-75.
[7] Bazant ZP. Physical model for steel corrosion in concrete sea structures - theory. Journal of the Structural Division-ASCE. 1979;105:1137-53.
[8] Yang S, Li K, Li C-Q. Analytical model for non-uniform corrosion-induced concrete cracking. Mag Concrete Res. 2017:1-10.
[9] Li CQ. Life-cycle modelling of corrosion-affected concrete structures: Propagation. J Struct Eng-ASCE. 2003;129:753-61.
[10] Cao C, Cheung MMS, Chan BYB. Modelling of interaction between corrosion-induced concrete cover crack and steel corrosion rate. Corros Sci. 2013;69:97-109.
[11] Sanz B, Planas J, Sancho JM. An experimental and numerical study of the pattern of cracking of concrete due to steel reinforcement corrosion. Eng Fract Mech. 2013;114:26-41.
[12] Jang BS, Oh BH. Effects of non-uniform corrosion on the cracking and service life of reinforced concrete structures. Cem Concr Res. 2010;40:1441-50.
[13] Zhang J, Ling X, Guan Z. Finite element modeling of concrete cover crack propagation due to non-uniform corrosion of reinforcement. Constr Build Mater. 2017;132:487-99.
[14] Zhu X, Zi G. A 2D mechano-chemical model for the simulation of reinforcement corrosion and concrete damage. Constr Build Mater. 2017;137:330-44.
[15] Qiao D, Nakamura H, Yamamoto Y, Miura T. Crack patterns of concrete with a single rebar subjected to non-uniform and localized corrosion. Constr Build Mater. 2016;116:366-77.
[16] Val; DV, Chernin; L, Stewart MG. Experimental and Numerical Investigation of Corrosion-Induced Cover Cracking in Reinforced Concrete Structures. J Struct Eng. 2009;135:10.
[17] Chernin L, Val DV. Prediction of corrosion-induced cover cracking in reinforced concrete structures. Constr Build Mater. 2011;25:1854-69.
[18] Zhang W, Ye Z, Gu X. Effects of stirrup corrosion on shear behaviour of reinforced concrete beams. Struct Infrastruct E. 2016;13:1081-92.
[19] Chen E, Leung CKY. Finite element modeling of concrete cover cracking due to non-uniform steel corrosion. Eng Fract Mech. 2015;134:61-78.
[20] Xi X, Yang S. Time to surface cracking and crack width of reinforced concrete structures under corrosion of multiple rebars. Constr Build Mater. 2017;155:114-25.
[21] Šavija B, Luković M, Pacheco J, Schlangen E. Cracking of the concrete cover due to reinforcement corrosion: A two-dimensional lattice model study. Constr Build Mater. 2013;44:626-38.
[22] Chen A, Pan Z, Ma R. Mesoscopic simulation of steel rebar corrosion process in concrete and its damage to concrete cover. Struct Infrastruct E. 2016;13:478-93.
[23] Du X, Jin L, Zhang R. Modeling the cracking of cover concrete due to non-uniform corrosion of reinforcement. Corros Sci. 2014;89:189-202.
[24] Yang ST, Li KF, Li CQ. Numerical determination of concrete crack width for corrosion-affected concrete structures. Comput Struct. 2017.
[25] Farid Uddin AKM, Numata K, Shimasaki J, Shigeishi M, Ohtsu M. Mechanisms of crack propagation due to corrosion of reinforcement in concrete by AE-SiGMA and BEM. Constr Build Mater. 2004;18:181-8.
[26] Gálvez JC, Cendón DA, Planas J. Influence of shear parameters on mixed–mode fracture of concrete. Int J Fracture. 2002;118:163-89.

[27] Lens LN, Bittencourt E, d'Avila VMR. Constitutive models for cohesive zones in mixed-mode fracture of plain concrete. Eng Fract Mech. 2009;76:2281-97.
[28] Camanho PP, Davila CG, Moura MFd. Numerical Simulation of Mixed-Mode Progressive Delamination in Composite Materials. J Compos Mater. 2002;34:1415-38.
[29] Yang Z, Frank Xu X. A heterogeneous cohesive model for quasi-brittle materials considering spatially varying random fracture properties. Comput Method Appl M. 2008;197:4027-39.
[30] Caré S, Nguyen QT, L'Hostis V, Berthaud Y. Mechanical properties of the rust layer induced by impressed current method in reinforced mortar. Cem Concr Res. 2008;38:1079-91.
[31] Yang ST, Li KF, Li CQ. Non-uniform corrosion-induced reinforced concrete cracking: an anlytical approach. In: J. Kruis YT, B.H.V. Topping, editor. 15th International Conference on Civil, Structural and Environmental Engineering Computing. Prague, Czech Republic: Civil-Comp Press; 2015.
[32] Yuan Y, Ji Y. Modeling corroded section configuration of steel bar in concrete structure. Constr Build Mater. 2009;23:2461-6.
[33] Neville AM. Properties of concrete. Fourth ed. London: Pearson Education Limited; 2006.
[34] Hillerborg A, Modeer M, Petersson PE. Analysis of crack formation and crack growth in concrete by means of fracture mechanics and finite elements. Cem Concr Res. 1976;6:773-81.
[35] Kurumatani M, Terada K, Kato J, Kyoya T, Kashiyama K. An isotropic damage model based on fracture mechanics for concrete. Eng Fract Mech. 2016;155:49-66.
[36] Tabiei A, Zhang W. Cohesive element approach for dynamic crack propagation: Artificial compliance and mesh dependency. Eng Fract Mech. 2017;180:23-42.
[37] Kenane M, Benzeggagh ML. Mixed-mode delamination fracture toughness of unidirectional glass/epoxy composites under fatigue loading. Compos Sci Technol. 1997;57:597-605.
[38] Ren W, Yang Z, Sharma R, Zhang C, Withers PJ. Two-dimensional X-ray CT image based meso-scale fracture modelling of concrete. Eng Fract Mech. 2015;133:24-39.
[39] Wang X, Zhang M, Jivkov AP. Computational technology for analysis of 3D meso-structure effects on damage and failure of concrete. Int J Solids Struct. 2016;80:310-33.
[40] Trawiński W, Bobiński J, Tejchman J. Two-dimensional simulations of concrete fracture at aggregate level with cohesive elements based on X-ray μCT images. Eng Fract Mech. 2016;168:204-26.
[41] Xi X, Yang S, Li C-Q. A non-uniform corrosion model and meso-scale fracture modelling of concrete. Cem Concr Res. 2018;108:87-102.
[42] Dong W, Wu Z, Zhou X, Wang N, Kastiukas G. An experimental study on crack propagation at rock-concrete interface using digital image correlation technique. Eng Fract Mech. 2017;171:50-63.
[43] Tregger N, Corr D, Graham-Brady L, Shah S. Modeling the effect of mesoscale randomness on concrete fracture. Probabilist Eng Mech. 2006;21:217-25.
[44] Rao GA, Raghu Prasad BK. Influence of type of aggregate and surface roughness on the interface fracture properties. Mater Struct. 2004;37:328-34.
[45] Corr D, Accardi M, Graham-Brady L, Shah S. Digital image correlation analysis of interfacial debonding properties and fracture behavior in concrete. Eng Fract Mech. 2007;74:109-21.
[46] Hong L, Gu X, Lin F. Influence of aggregate surface roughness on mechanical properties of interface and concrete. Constr Build Mater. 2014;65:338-49.

[47] Caré S, Nguyen QT, Beddiar K, Berthaud Y. Times to cracking in reinforced mortar beams subjected to accelerated corrosion tests. Mater Struct. 2009;43:107-24.
[48] Andrade C, Molina FJ, Alonso C. Cover cracking as a function of rebar corrosion: Part 1-experiment test. Mater Struct. 1993;26:453-4.

LIST OF TABLES

Table 1 Three-segment gradation of aggregate size distribution [33]

Aggregate size (mm)	Fraction (%)
2.40-4.76	20.2 %
4.76-9.52	39.9%
9.52-19.05	39.9%

Table 2 Values for geometric and mechanical parameters for different phases

Description	**Symbol**	**Values**
Cover thickness	C	40 mm
Diameter of steel bars	D	16 mm
Young's modulus of aggregate	E_{Agg}	70 GPa [38]
Young's modulus of mortar	E_{Mor}	25 GPa [38]
Poisson's ratio of aggregate	ν_{Agg}	0.2 [38]
Poisson's ratio of mortar	ν_{Mor}	0.2 [38]
Tensile strength of mortar	$\sigma_{n,Mor}$	2.6 MPa [43, 44]
Tensile strength of ITZ	$\sigma_{n,ITZ}$	1.3 MPa [43, 44]
Shear strength of mortar	$\sigma_{s,Mor}$	2.6 MPa [43, 44]
Shear strength of ITZ	$\sigma_{s,ITZ}$	1.3 MPa [43, 44]
Mode I fracture energy of mortar	$G_{I,Mor}$	40 N/m [43, 44]
Mode I fracture energy of ITZ	$G_{I,ITZ}$	17 N/m [43, 44]
Mode II fracture energy of mortar	$G_{II,Mor}$	80 N/m [43, 44]
Mode II fracture energy of ITZ	$G_{II,ITZ}$	34 N/m [43, 44]

Table 3 Values used for comparison and validation

Description	**Values**
Cover thickness	20 mm [48]
Diameter of steel bars	16 mm [48]
Tensile strength of concrete	3.5 MPa [48]
Young's modulus of aggregate	70 GPa [38]
Young's modulus of mortar	25 GPa [38]
Poisson's ratio of aggregate	0.2 [38]
Poisson's ratio of mortar	0.2 [38]
Cohesive strength of mortar	6 MPa [38]
Cohesive strength of ITZ	2 MPa [38]
Fracture energy of mortar	60 N/m [38]
Fracture energy of ITZ	30 N/m [38]

LIST OF FIGURES

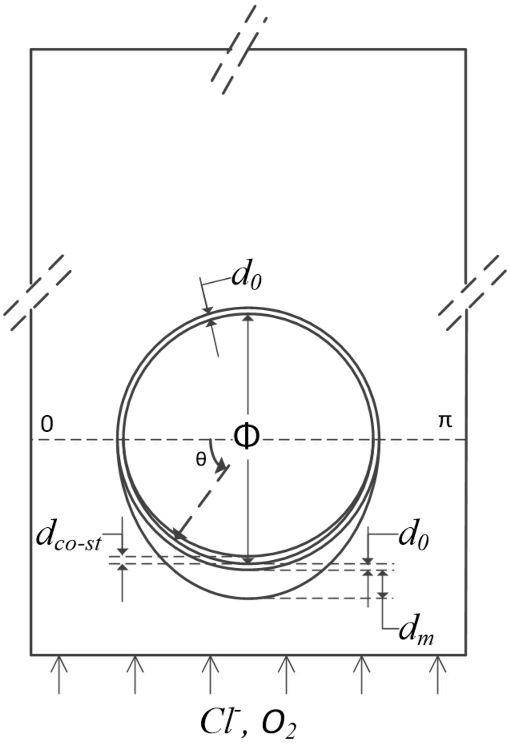

Figure 1 Non-uniform corrosion model

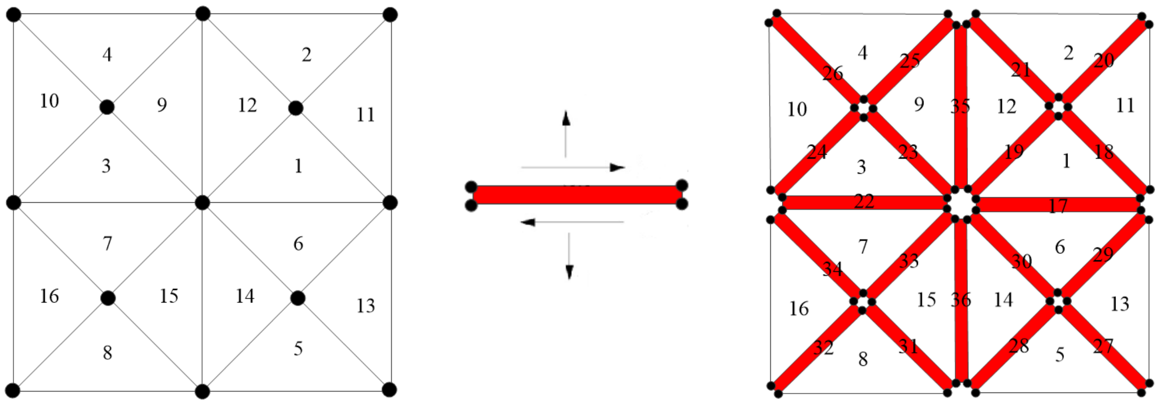

(a) (b) (c)

Figure 2 Insertion process of cohesive elements: (a) initial mesh; (b) inserted cohesive element based on newly created nodes; and (c) mesh after insertion of cohesive elements

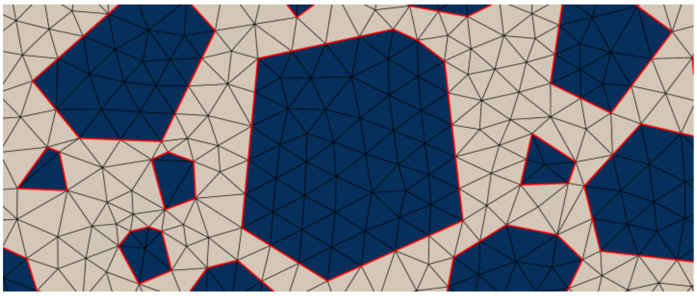

[redacted]

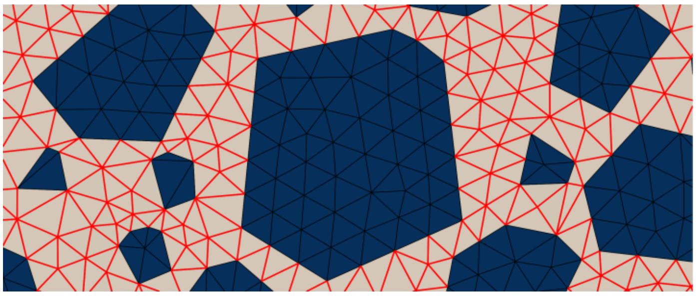

[redacted]

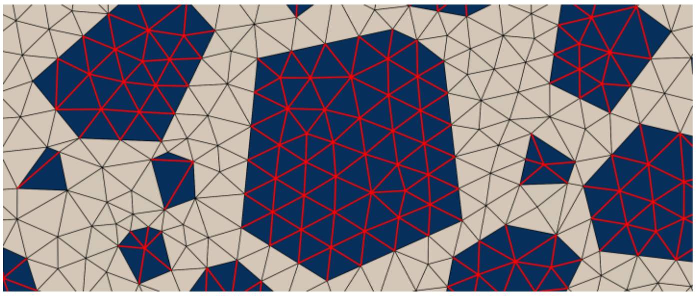

[redacted]

Figure 3 Inserted cohesive elements in the FE mesh

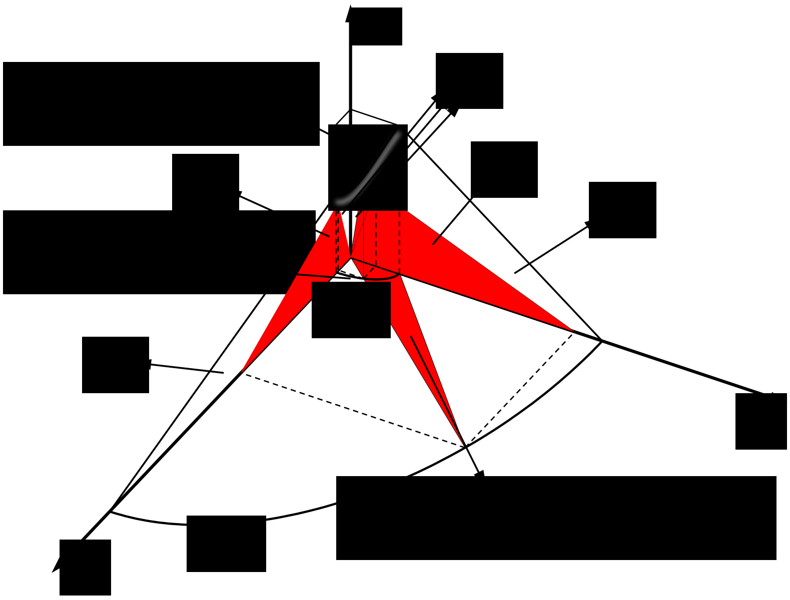

(a) Mixed-mode response model

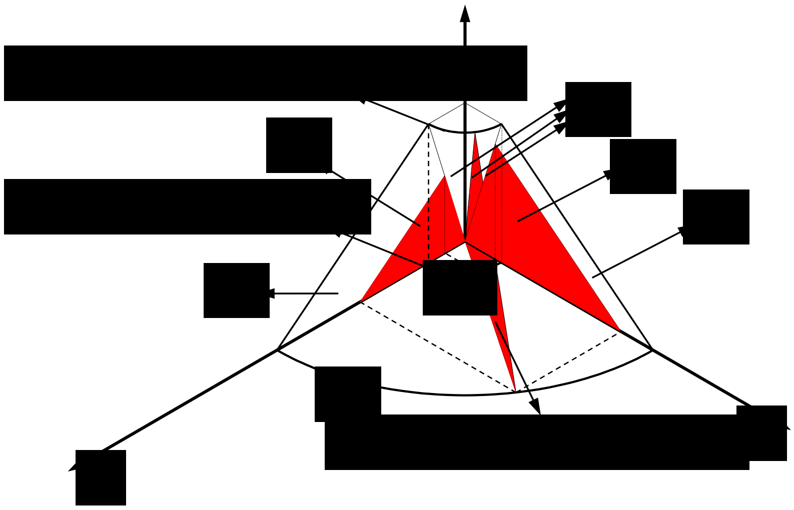

(b) A special case for $\sigma_n^0 = \sigma_s^0$ and $G_I = G_{II}$

Figure 4 Constitutive model for mixed-mode fracture

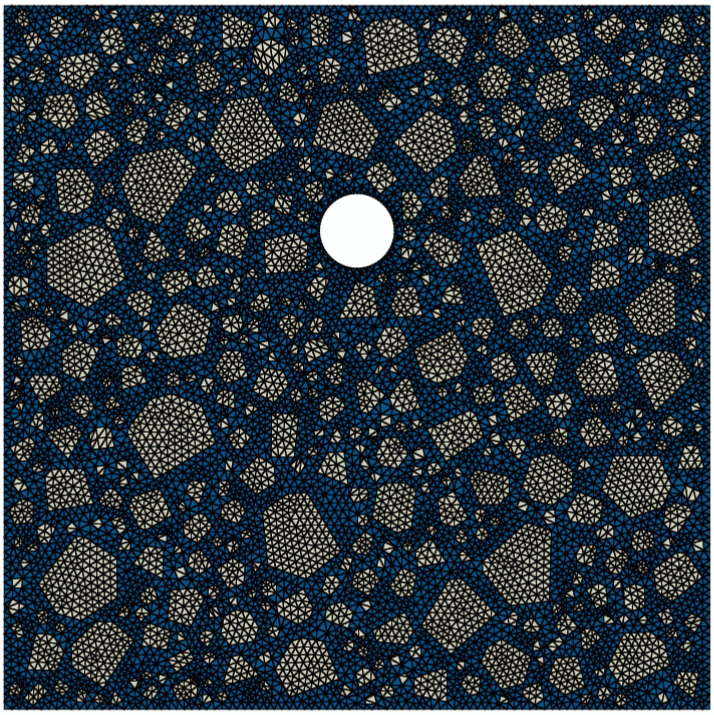

Figure 5 Typical Mesh for the worked example

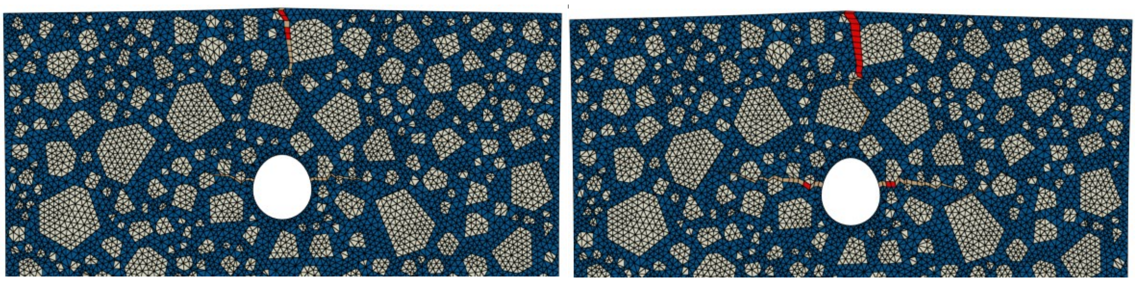

(a) $d_m = 31.50\ \mu\text{m}$ (b) $d_m = 46.82\ \mu\text{m}$

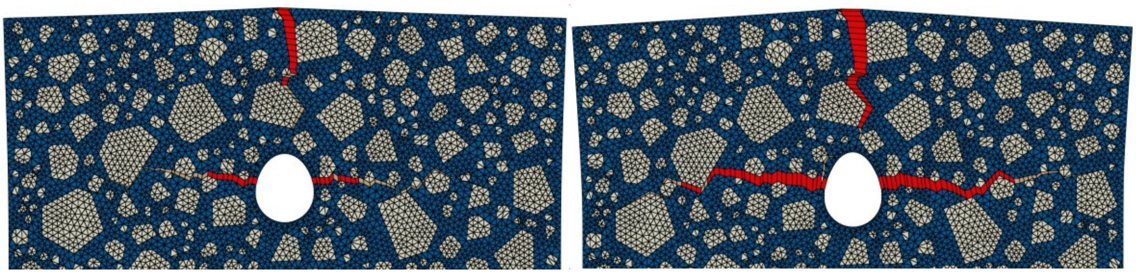

(c) $d_m = 84.34\ \mu\text{m}$ (d) $d_m = 96.21\ \mu\text{m}$

Figure 6 Crack propagation in concrete induced by non-uniform corrosion of reinforcement

（Deformation scale 10 ）

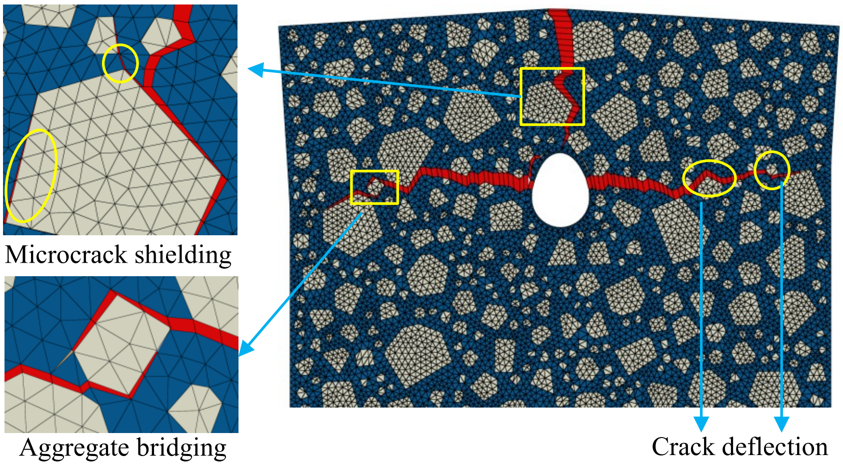

Figure 7 Toughening mechanisms captured in the meso-scale model

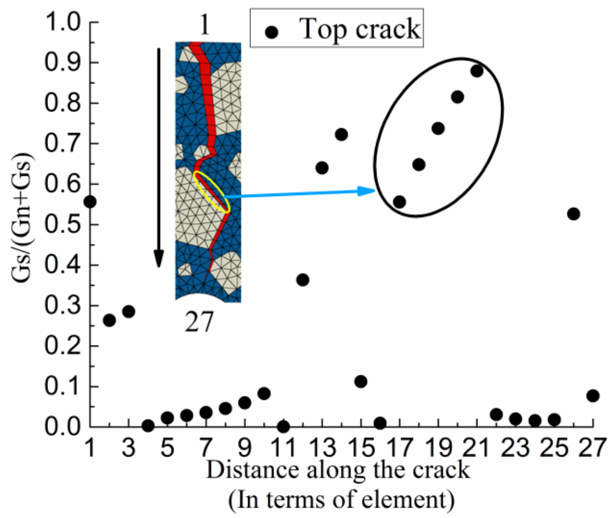

(a)

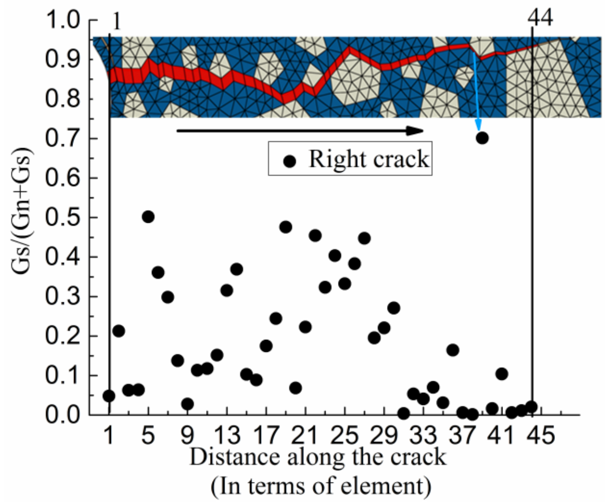

(b)

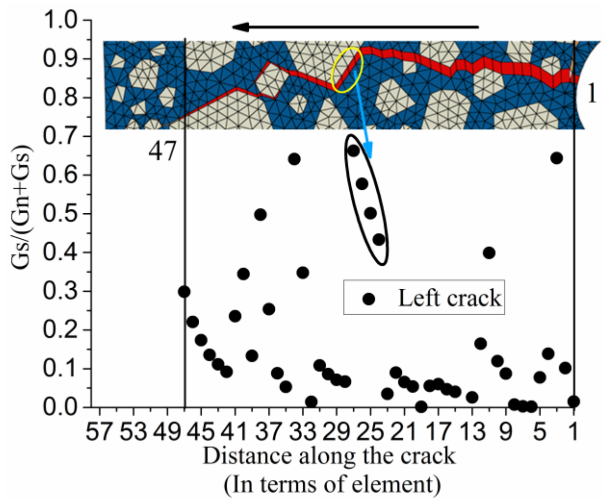

(c)

Figure 8 Contributions of shear on the mixed-mode fracture

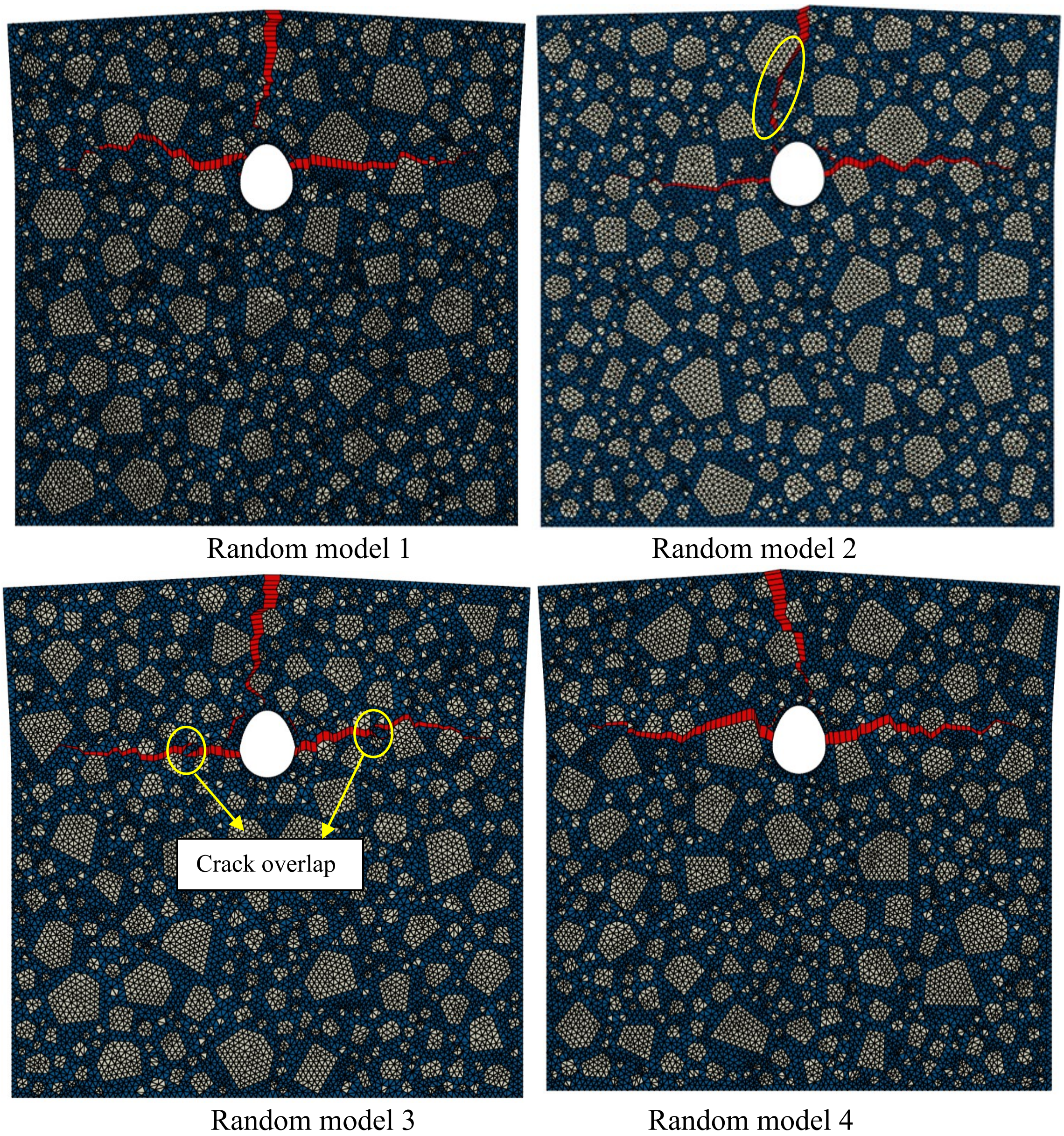

Figure 9 Crack patterns of 4 random meso-scale models

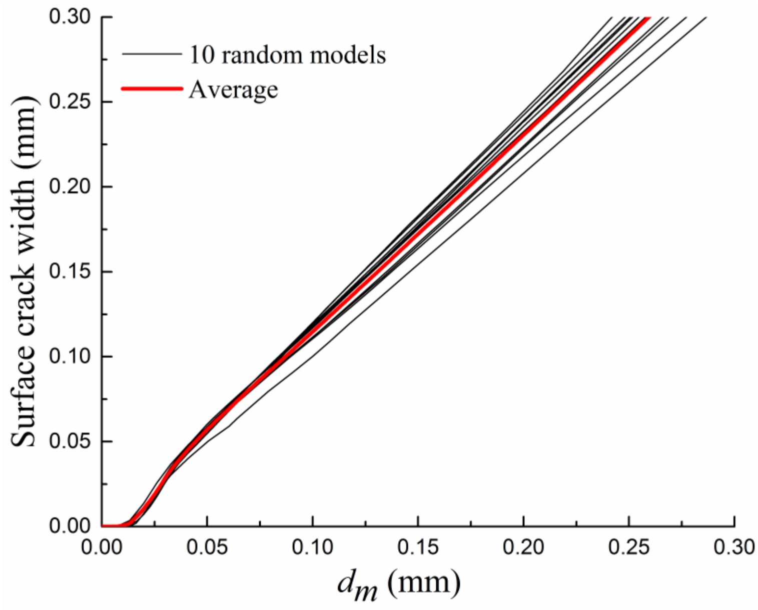

Figure 10 The crack width as a function of corrosion expansion displacement for 10 random meso-scale models

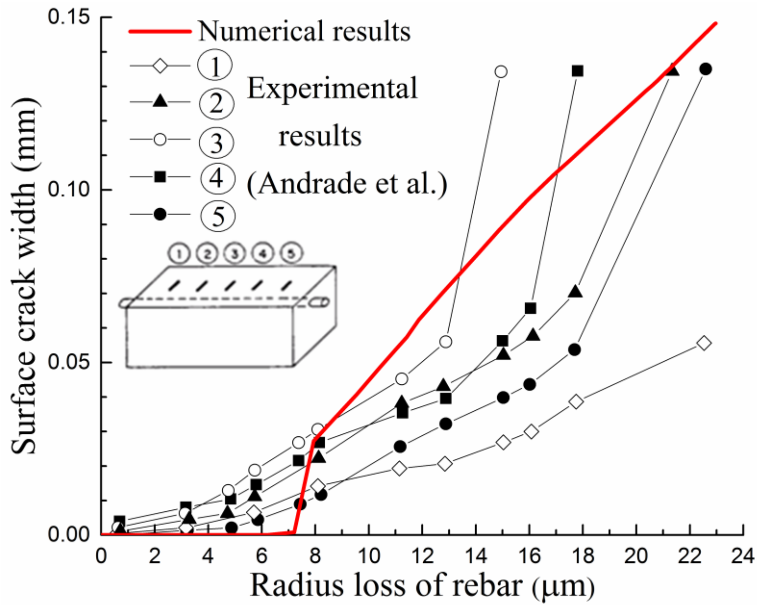

Figure 11 Experimental verification of the crack width development

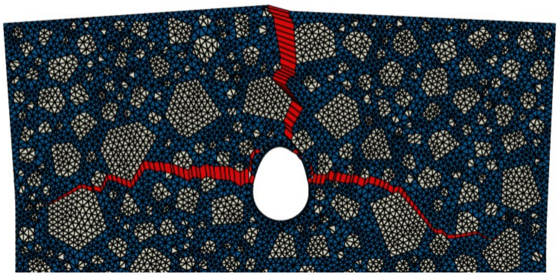

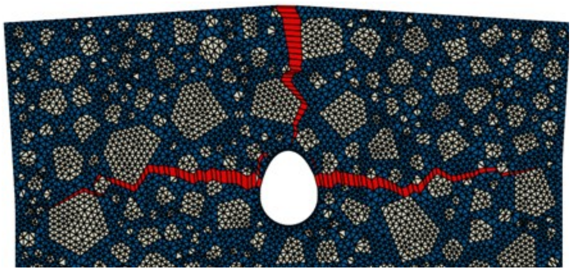

（a）$G_{II}=G_I$ （b）$G_{II}=2G_I$

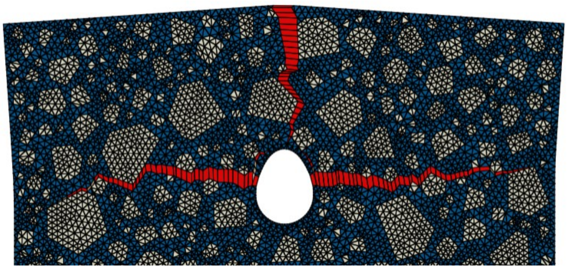

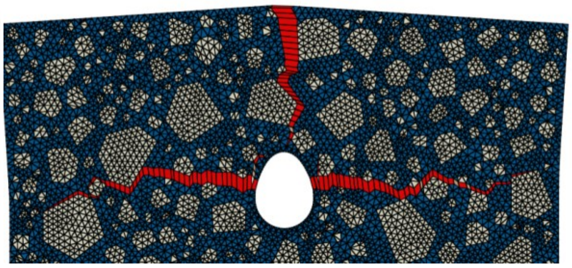

（c）$G_{II}=10G_I$ （d）$G_{II}=20G_I$

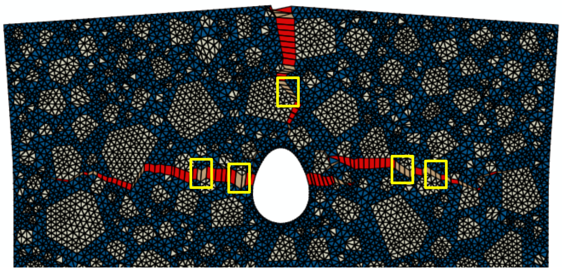

（e）$G_{II}=100G_I$

Figure 12 Crack patterns under different fracture energies of Mode II

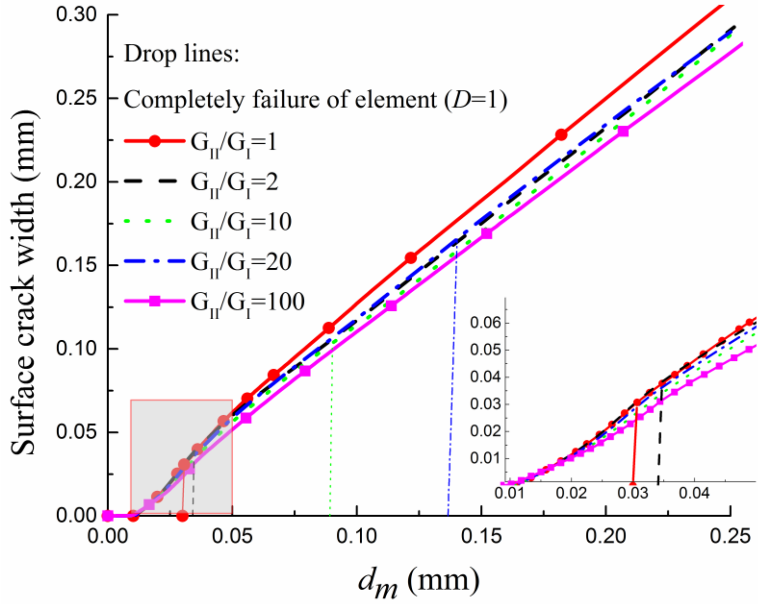

Figure 13 The crack width affected by fracture energies of Mode II

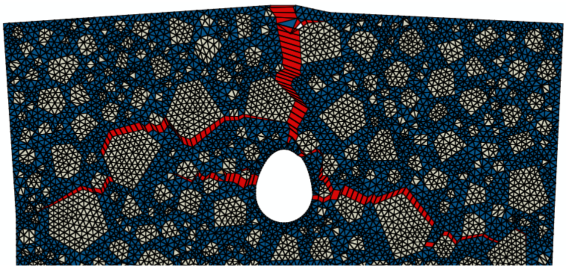

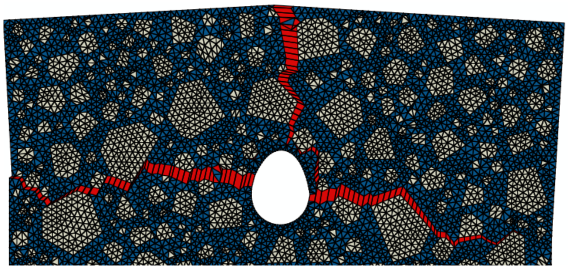

(a) $\sigma_{t,ITZ}/\sigma_{t,Mor}=1/8;\sigma_{s,ITZ}/\sigma_{s,Mor}=1/8$ (b) $\sigma_{t,ITZ}/\sigma_{t,Mor}=1/4;\sigma_{s,ITZ}/\sigma_{s,Mor}=1/4$

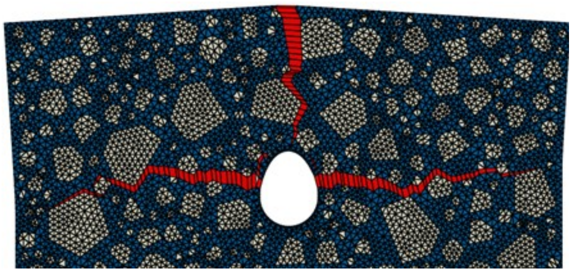

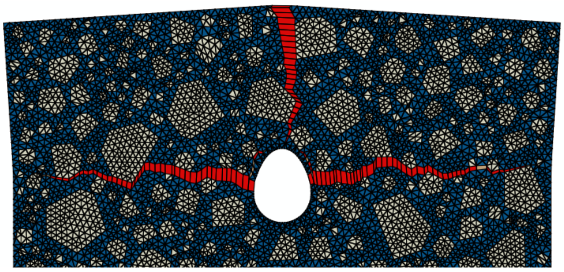

(c) $\sigma_{t,ITZ}/\sigma_{t,Mor}=1/2;\sigma_{s,ITZ}/\sigma_{s,Mor}=1/2$ (d) $\sigma_{t,ITZ}/\sigma_{t,Mor}=3/4;\sigma_{s,ITZ}/\sigma_{s,Mor}=3/4$

Figure 14 Crack patterns under different tensile and shear strengths of ITZ

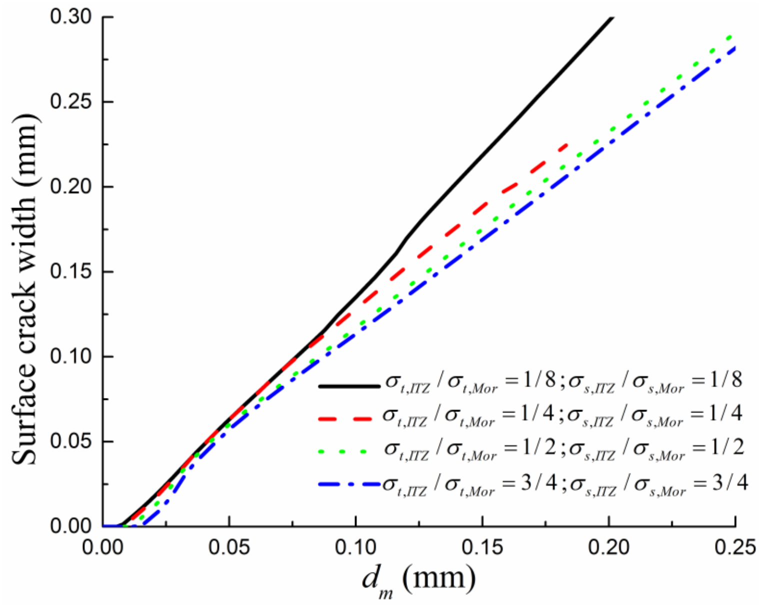

Figure 15 The crack width developments under different tensile and shear strengths of ITZ

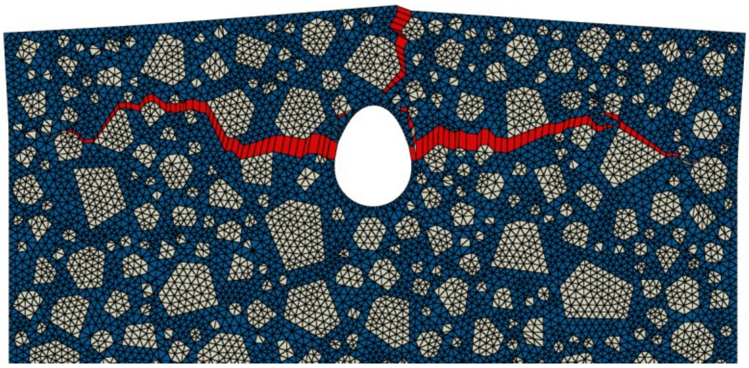

(a) *C*=20 mm

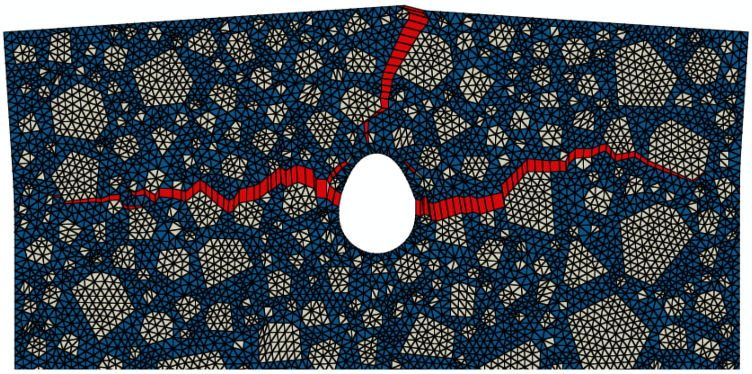

(b) *C*=30 mm

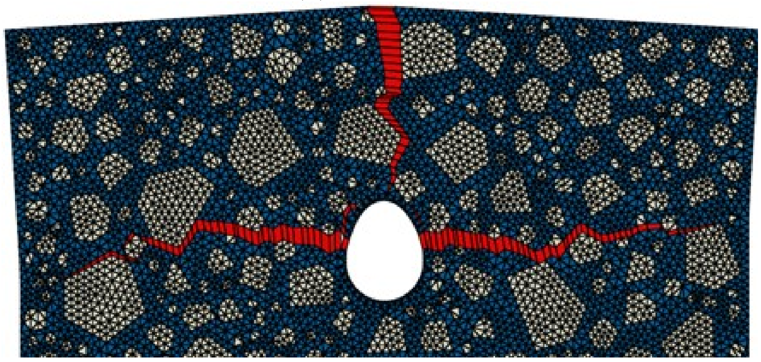

(c) *C*=40 mm

Figure 16 Crack patterns for different thicknesses of concrete cover

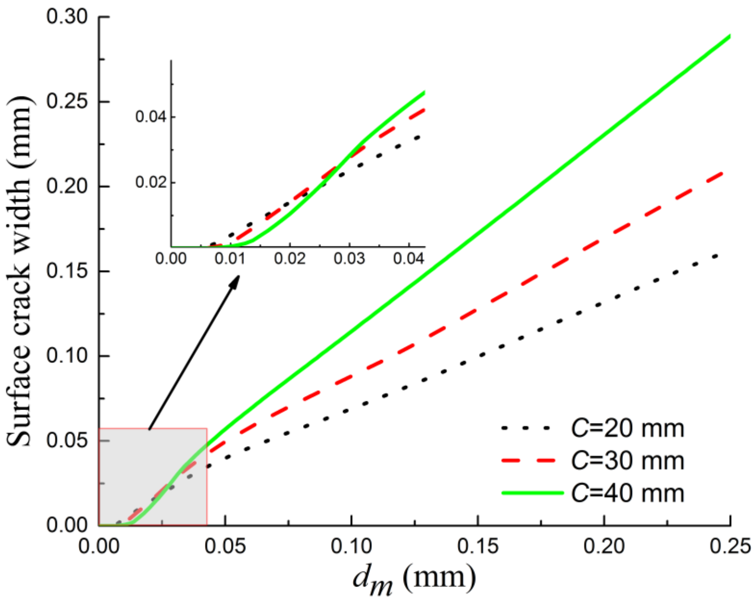

Figure 17 The crack width developments for different thicknesses of concrete cover

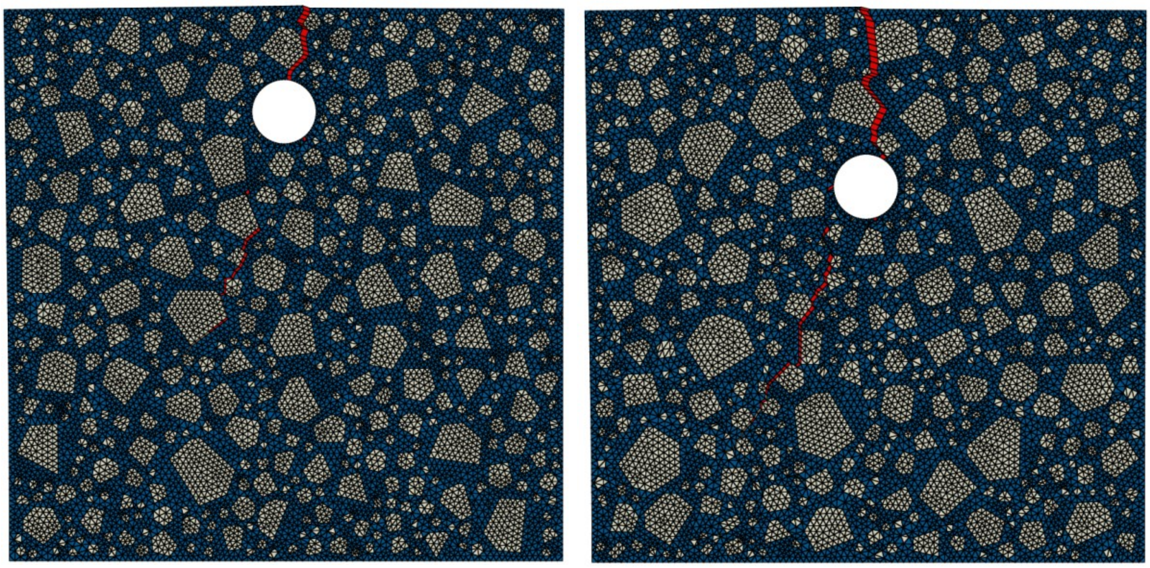

(a) *C*=20 mm & Uniform corrosion (b) *C*=40 mm & Uniform corrosion

Figure 18 Crack patterns of concrete cover induced by uniform corrosion of reinforcement

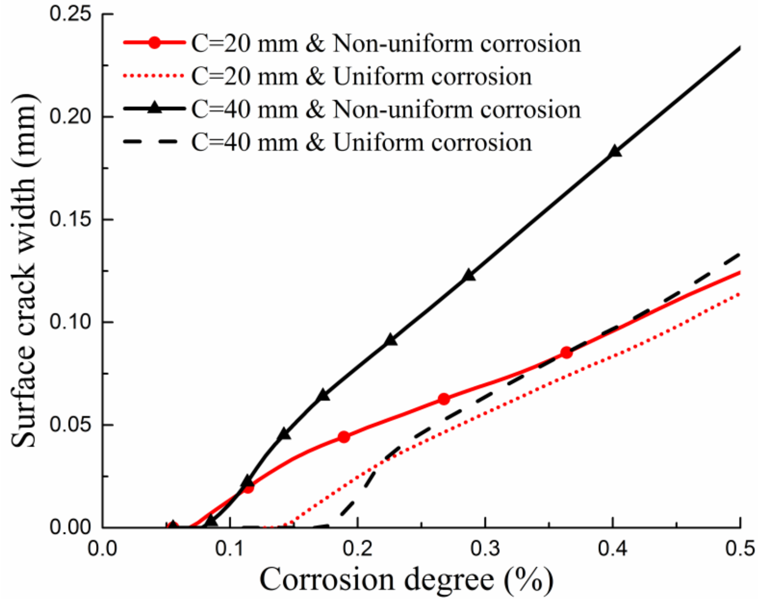

Figure 19 The crack width developments with corrosion degree